Lattice dynamics in $PbMg_{1/3}Nb_{2/3}O_3$

S. A. Prosandeev,* E. Cockayne, and B. P. Burton
Ceramics Division, Materials Science and Engineering Laboratory, National Institute of Standards and Technology, Gaithersburg, Maryland 20899-8520, USA

S. Kamba and J. Petzelt
Institute of Physics, Academy of Science of the Czech Republic, Na Slovance, 2, 18221 Prague 8, Czech Republic

Yu. Yuzyuk* and R. S. Katiyar
Department of Physics, University of Puerto Rico, P.O. Box 23343, San Juan, Puerto Rico 00931-3343, USA

S. B. Vakhrushev
A. F. Ioffe Physical-Technical Institute, 194021 St. Petersburg, Russia
(Received 13 May 2004; published 28 October 2004)

Lattice dynamics for five ordered $PbMg_{1/3}Nb_{2/3}O_3$ supercells were calculated from first principles by the frozen phonon method. Maximal symmetries of all supercells are reduced by structural instabilities. Lattice modes corresponding to these instabilities, equilibrium ionic positions, and infrared reflectivity spectra were computed for all supercells. Results are compared with our experimental data for a chemically disordered PMN single crystal.

DOI: 10.1103/PhysRevB.70.134110 PACS number(s): 63.10.+a, 63.20.Dj

I. INTRODUCTION

Lead magnesium niobate $PbMg_{1/3}Nb_{2/3}O_3$ (PMN) is an ABO_3-perovskite that exhibits relaxor ferroelectric (RFE) properties, such as a broad, frequency sensitive, dielectric permittivity peak at T_{max} near room temperature.[1,2] It was originally suggested that RFE properties are associated with a "diffuse phase transition" that reflects a *random* spatial distribution of Curie temperatures,[1] originating from chemical inhomogeneities; however, the implied chemical segregation of Mg^{2+} and Nb^{5+} ions on perovskite B-sites has not been observed. Rather, transmission electron microscopy (TEM) indicates chemical short-range order (SRO) such that 1:1 ordered domains, 20–50 Å across, are embedded in a disordered matrix.[3] Thus, the microstructure is characterized by fluctuations of a 1:1 chemical order parameter on the 20–50 Å length scale, and not by compositional fluctuations about Mg:Nb=1:2, as previously suggested.[4,5]

The "random site model (RSM)" for the ordered domains,[6–10] has NaCl type Mg/Nb ordering with one B-site occupied by Nb^{5+}, and the other by a random mixture of $1/3\ Nb^{5+}+2/3\ Mg^{2+}$. Note that the term "random-site model" is only used for an idealized model. The term "1:1 phase" is used for real crystals that presumably have some SRO chemical correlations which are deviations from *randomness* on the Mg^{2+}-rich sites.

Burns and Dacol[11] observed that the refractive index of PMN departs significantly from a linear temperature dependence below a characteristic temperature, $T_B \sim 630$ K (Burns temperature). They interpreted these data as indicating that polar nanoclusters (PNC) condense at $T<T_B$; and T_B is now generally accepted as the crossover between RFE and paraelectric (PE) states. Recent TEM studies[12,13] have attempted to correlate chemical SRO with PNC.

Chemical SRO makes PMN inhomogeneous at a length-scale that affects vibrational mode activities. Mode activities in inhomogeneous media are determined by the range of interatomic forces, typically a few lattice parameters, and they do not depend on the wavelength of the probing radiation. However, the probing radiation wavelength does determine the volume in which the spectroscopic response is averaged. If, as in PMN, the inhomogeneities are smaller than the wavelength, an effective medium approach is justified.

Room-temperature IR reflectivity spectra of PMN single crystals were first published in the 1970s.[11,14] Karamyan reported three polar modes, characteristic of cubic perovskites. Burns and Dacol, however, reported many more modes, which they explained as "two-mode behavior." Subsequent studies of PMN ceramics[15] agreed with Karamyan's spectrum, but the resolution was poor.

The interpretation of Raman spectra from PMN is also controversial (e.g., Refs. 16 and 17). The Raman spectra of PMN and PST are similar,[16,18] and it was assumed that the main features of both reflect $Fm\bar{3}m$ symmetry (locally for PMN) as in the 1:1 phase. In $Fm\bar{3}m$, the Raman active modes are A_{1g}, E_g, and $2F_{2g}$: A_{1g} and E_g modes are observable in parallel (VV) geometry; $2F_{2g}$ modes are observable in crossed-polarized (VH) geometry. Polarized Raman studies and Raman spectral intensities support TEM results suggesting that PMN has 1:1 chemical SRO in a disordered matrix.

The objectives of this study are: (1) to perform a comparative supercell stability analyses in PMN, including symmetry-breaking relaxations [i.e., finding ground states (GS) with symmetries that are lower than those dictated by chemical ordering]; (2) to compute the lattice dynamics for the same set of ordered PMN supercells, and to compare the results with experimental data, e.g., by comparing simulated IR reflectivity spectra with the experimental one. The goal is to find which ordered supercell most closely approximates the experimental case of local 1:1 order.

TABLE I. Parameters of the polar phonon modes in PMN, from fits of IR and THz spectra at 20 and 300 K. Mode frequencies ν_{TOi}, ν_{LOi} and dampings γ_{TOi},γ_{LOi} are in cm^{-1}, $\Delta\varepsilon_i$ is dimensionless, $\varepsilon_\infty=5.83$.

	20 K					300 K				
No	ν_{TOi}	γ_{TOi}	ν_{LOi}	γ_{LOi}	$\Delta\varepsilon_i$	ν_{TOi}	γ_{TOi}	ν_{LOi}	γ_{LOi}	$\Delta\varepsilon_i$
CM	36.2	44.8	62.5	56.2	129.2	24.2	69.2			539.1
1	65.0	15.2	67.1	18.2	0.6					
(TO1) 2	88.2	22.0	122.9	32.7	15.7	54.3	38.3	102.0	17.3	79.6
3	245.5	76.9	264.1	49.0	11.8	227.7	85.1	282.6	65.0	17.7
4	272.3	59.4	382.1	60.9	4.1	287.7	55.0	334.2	45.0	0.9
5	385.1	41.2	406.3	21.4	0.1	336.2	47.5	397.7	7.5	0.13
6	434.0	93.7	455.3	22.0	0.3	427.9	55.7	442.3	35.4	0.2
7	547.9	80.6	703.0	22.9	1.8	545.4	105.1	703.0	62.5	2.0

II. INFRARED SPECTRA

IR and THz measurements were performed on a PMN single crystal, down to liquid helium temperatures, where all polar modes are well distinguished. A disk of 9 mm diameter and 3 mm thickness was cut from a PMN single crystal, and polished for specular IR reflectivity measurements. A time-domain THz spectrometer was used to determine the complex dielectric response $\varepsilon^*(\nu)$ in the submillimeter and near-millimeter ranges. This spectrometer uses femtosecond laser pulses to generate THz radiation via optical rectification on a ZnTe single crystal, with an electro-optic sampling detection technique. Low-temperature spectra were taken in transmission configuration from 100 to 900 GHz, where the thin (100 μm thick) plane-parallel plate was semitransparent. Room temperature dielectric response up to 2.5 THz was calculated from the THz reflectance data.[19] The unpolarized near-normal reflectivity spectra were taken with a Fourier transform IR (FTIR) spectrometer Bruker IFS 113v at $20 \leqslant T \leqslant 300$ K in the spectral range 20–650 cm^{-1}; room-temperature spectra were measured up to 4000 cm^{-1}.

IR reflectivity spectra were fitted together with complex dielectric THz spectra using a generalized-oscillator model with the factorized form of the complex dielectric function:

$$\varepsilon^*(\nu) = \varepsilon'(\nu) - i\varepsilon''(\nu) = \varepsilon_\infty \prod_{j=1}^{n} \frac{\nu_{LOj}^2 - \nu^2 + i\nu\gamma_{LOj}}{\nu_{TOj}^2 - \nu^2 + i\nu\gamma_{TOj}}, \quad (1)$$

where the dielectric function is related to reflectivity $R(\nu)$ by

$$R(\nu) = \left| \frac{\sqrt{\varepsilon^*(\nu)} - 1}{\sqrt{\varepsilon^*(\nu)} + 1} \right|^2. \quad (2)$$

ν_{TOj} and ν_{LOj} are the transverse optic and longitudinal optic (LO) frequency of the jth mode, respectively; γ_{TOj} and γ_{LOj} the corresponding damping constants. The high-frequency (electronic) permittivity ε_∞ was obtained from the frequency-independent 300 K reflectivity above the phonon frequencies. The temperature dependence of ε_∞ is usually very small and was neglected in our fits. The TO1 mode was fit to the more accurate FTIR reflectivity. Below 30 cm^{-1}, the THz data are more accurate than the FTIR data, so they were given greater weight in the fit. The results are shown in Table I. In particular, the TO1 frequency follows the Cochran law and phonon frequency shifts from 88 cm^{-1} at 20 K down to 54 cm^{-1} at 300 K (Ref. 9). Therefore we can call it a soft mode.

The low-frequency part [so-called central mode (CM)] of the 300 K spectrum, below polar phonon frequencies, was fit to an overdamped three parameter oscillator model. This fit does not explain the experimental low-frequency permittivity which is one order of magnitude higher, owing to broad dispersion between the audio- and microwave-frequency ranges.[19–21] It is well known that the distribution of relaxation frequencies in this dispersion reaches up to the submillimeter range at room temperature.[19,21] The CM slows down, broadens on cooling and, at 20 K, is beyond our spectral range (Ref. 19). At 20 K, a new heavily damped excitation appears near 30 cm^{-1} together with a weak mode near 65 cm^{-1} (Table I).

III. RAMAN SPECTRA

Raman spectra were excited with polarized light from a coherent INNOVA 99 Ar^+ laser ($\lambda=514.5$ nm) and analyzed with a Jobin Yvon T64000 spectrometer, that was equipped with a charge coupled device (CCD). Polarized Raman spectra were measured in backscattering geometry on the ($1\times2\times3$ mm^3) sample.

Incident light was focused to a spot size of ~3 μm in diameter, as measured by optical microscopy. Low- and high-temperature micro-Raman measurements were made with a Linkam FDCS 196 cryostat and Linkam TS1500 hot stage, respectively. Measured Raman spectra were corrected for the Bose-Einstein temperature factor.

Figure 1 shows the temperature dependence of parallel (VV) and crossed (VH) polarized Raman spectra in the temperature interval 77–700 K. The main feature is that the frequencies of all observed peaks are only weakly temperature-dependent. Below 270 K, a partial depolarization occurs, due to the leakage of intense peaks from the VV spectrum to VH.

All peaks are best resolved at low temperature, though most of them can be traced up to 1000 K. As shown in Fig. 1 the VV spectrum exhibits: a band at 54 cm^{-1}; an envelope of strongly overlapping bands between 100 and 350 cm^{-1}; a very weak broad band at about 430 cm^{-1}, that is clearly seen

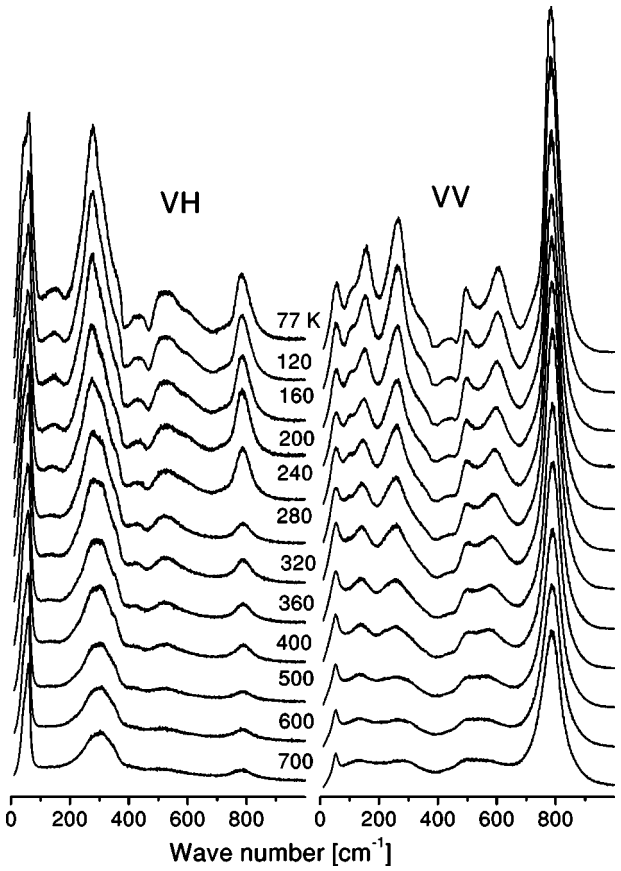

FIG. 1. Temperature dependence of Raman intensity (corrected for the temperature factor).

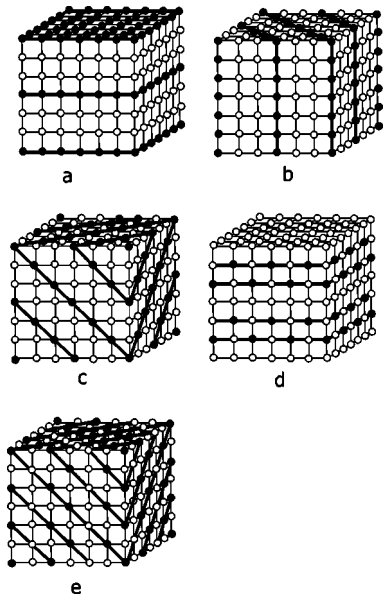

FIG. 2. PMN supercell: $[001]_{NNM}$ (a), $[110]_{NNM}$ (b), $[111]_{NNM}$ (c), $[001]_{NCC'}$ (d), $[111]_{NT}$ (e).

only at low temperature; strongly overlapping bands in the 500–600 cm^{-1} range; and a very intense band at 780 cm^{-1}. In the VH spectrum the low-frequency band is a doublet (45 and 62 cm^{-1}) and intermediate bands in the 100–350 cm^{-1} range are also strongly overlapping. The intensity of the 780 cm^{-1} band increases abruptly at about 270 K, just below T_{max}. The 780 cm^{-1} band was interpreted as a fully symmetrical (A_{1g}) stretching vibration of oxygen octahedra that originates from 1:1 chemically ordered regions.[22] The 500–600 cm^{-1} wide band, usually associated with E_g Raman active vibration, increases splitting when T decreases[17] below 350 K, and as would occur with local $I4mm$ symmetry but not $R3m$ (Ref. 23). Actually, any monoclinic distortions split this mode also. Perfect 1:1 chemical ordering implies four Raman-active modes: $A_{1g}+E_g+2F_{2g}$. The measured Raman spectra are much more complicated, however, which suggests that both chemical SRO, and local symmetry reductions from lattice instabilities, activate Raman modes that are inactive under $Fm\bar{3}m$ selection rules.

IV. COMPUTATIONAL METHODS

Density functional theory (DFT) calculations for PMN were done with the Vienna *ab initio* simulation package (VASP).[24,25] A plane wave basis set was used for electronic wave functions and ultrasoft pseudopotentials were employed.[26] Exchange and correlation energies were calculated with the local density approximation (LDA). Lattice-dynamical force constants were calculated via the frozen phonon method. Berry's phase analyses were used to compute dynamical charges, as implemented in VASP by Marsman. In all cases, we used a 495 eV cutoff for the plane wave energy, 10^{-7} eV per cell convergence of total energies, $4\times4\times4$ Monkhorst-Pack k-point grids for the 30-ion supercells, and $6\times6\times6$ grids for the 15-ion supercells.

A. Ordered supercells

Ordered supercells with PMN stoichiometry require $15n$ atoms ($n=1,2,\ldots$). The calculations presented here are for three 15-atom cells, and two 30-atom cells (Fig. 2): (a) $[001]_{NNM}$; (b) $[110]_{NNM}$; (c) $[111]_{NCM}$; (d) $[001]_{NNC'}$; (e) $[111]_{NT}$. Here: subscript N=a Nb layer parallel to (h,k,l); M=a Mg layer parallel to (h,k,l); C=a chessboard ordered layer, i.e., a $Mg_{1/2}Nb_{1/2}$-layer or $(001)_{1:1}$-layer; C'=a chessboard ordered $(001)_{1:1}$-layer that is displaced by $[1/2,0,0]$ relative to an adjacent C-layer; T=a $(111)_{2:1}$-layer of composition $Mg_{2/3}Nb_{1/3}$, which is triangularly-ordered [Fig. 3(a)]. The $[001]_{NCC'}$ structure (d) has $(001)_{Nb}$ layers that alternate with CC' double layers (NaCl-type blocks). This structure was proposed[27] as a possible cation ordering GS for PMN, however the stability analyses reported below indicate that the $[111]_{NT}$ structure is lower in energy. The $[111]_{NT}$ structure has $(111)_{Nb}$ layers alternating with $(111)_{Mg_{2/3}Nb_{1/3}}$ layers, and, as such, is an ordered approximate of the 1:1 "random-site model." Although labeled "NT" for Nb layer/triangular layer alternation, the cation arrangement in the 2:1 layers depends on the layer's orientation. In Fig. 2(e), there are triangularly-ordered layers perpendicular to [111] and $[\bar{1}11]$ and striped layers [Fig. 3(b)] perpendicular to [111] and $[\bar{1}11]$.

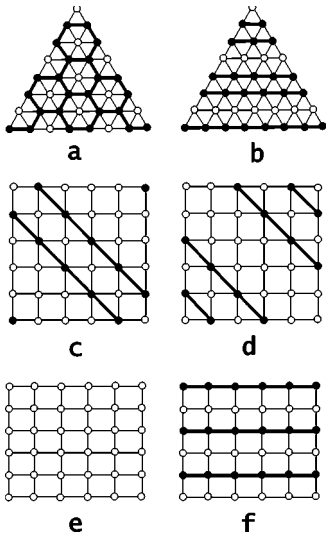

FIG. 3. Filling the $Mg_{2/3}Nb_{1/3}$ layers in the $[111]_{NT}$ structure with Mg (black circles) and Nb (open circles) in the direction of (a–b) [111], (c–d) [001], and (e–f) [110].

For each ordered supercell, two space group symmetries, and two corresponding energies, are given in Table II: G_{Chem} indicates the space group symmetry dictated by chemical ordering without additional displacive instabilities; G_{SSS} is space group of the lower symmetry "structurally stable state." The SSS was determined by applying random perturbations to the atomic positions, and then relaxing the system until full convergence. The difference $\Delta E_{\mathrm{SSS}} - \Delta E_{\mathrm{Chem}}$ is referred to as the relaxation energy.

In general, $G_{\mathrm{SSS}} \subset G_{\mathrm{Chem}} \subset Pm\bar{3}m$, and $\Delta E_{\mathrm{SSS}} < \Delta E_{\mathrm{Chem}}$. Randomness of the initial perturbation does not guarantee that the SSS is in fact the ground-state of the system ($G_{\mathrm{SSS}} = G_{\mathrm{GS}}$), but it does guarantee that it is, at least, metastable.

B. Short-range order and lattice averaged spin products

Chemically ordered, disordered, and random configurations can be quantitatively analyzed with respect to their short-range order (SRO) correlations, and one can answer such questions as: which configuration is most similar to the random state[28–30] or, more relevant for this work, which is most similar to the random site model (RSM)? The procedure is to calculate a lattice averaged spin product (LASP), $\overline{\Pi}(r,t)_S$, for each structure (S) and cluster (r,t):

$$\overline{\prod}(r,t)_S = M(0)\xi(0)_S + M(1)\xi(1)_S + M(2,1)\xi(2,1)_S \cdots + M(8)\xi(8)_S. \quad (3)$$

Here, $\overline{\Pi}(r,t)_S$ is the product between multiplicities, $M(r,t)$, for r-body clusters of type t and correlation functions, $\xi(r,t)$, for the clusters. The parameter $r=1,2,\ldots$, is the number of sites in the cluster ($1=$site, $2=$pair$\ldots 8=$cube), and t is an arbitrary index (e.g., $t=2$ for an r-body cluster of type 2). In a two-component system, there is a one-to-one correspondence between symmetrically distinct clusters and (r,t) clusters (symmetrically distinct in the high-symmetry phase). The correlation function for any cluster is $\xi(r,t) = \langle \sigma_i \sigma_j \cdots \sigma_r \rangle$, where: $\langle \sigma_i \sigma_j \cdots \sigma_r \rangle$ is an ensemble average; $\sigma = 1$ for Mg; and $\sigma = -1$ for Nb. In general: $\xi(0)=1$; $-1 \leqslant \xi(1) \leqslant 1$ for the site (point) correlation; $-1 \leqslant \xi(2,1) \leqslant 1$ for the first nn pair; $-1 \leqslant \xi(2,2) \leqslant 1$ for the second nn pair, etc. The $\{\xi(r,t)\}$ sets listed in Table III are truncated at the cube-approximation; i.e., only the correlations for cubes and their subclusters, are included. Indices in column 1 identify symmetrically distinct subclusters of the cube in space group $P\bar{3}m$, labeled as in Fig. 4; column 2 lists the $M(r,t)$; columns 3–9 list the $\xi(r,t)$ for the random state, RSM, and the [001], [111], [110], and $[111]_{NCC'}$ supercells, respectively.

The $\{\xi(r,t)\}$ sets for the [001], [111], [110], and $[111]_{NCC'}$ structures were calculated by counting the distributions of distinct cube-cluster configurations in each structure, and the distribution of subclusters therein. Correlation functions for the random configuration were calculated using

$$x(8)_{ijklmnop} = x(1)_i\, x(1)_j\, x(1)_k\, x(1)_l\, x(1)_m\, x(1)_n x(1)_o\, x(1)_p, \quad (4)$$

where $x(8)_{ijklmnop}$ is the probability that a cube (8-body cluster) has configuration $ijklmnop$, and $x(1)_i$ is the probability of finding atom i on the site labeled i in Fig. 4. That is, $x(1)_i = 2/3$ when Nb occupies site i, and $x(1)_i = 1/3$ when Mg occupies site i. Cluster algebra [relationships between the $x(r,t)$ and $\xi(r,t)$] for a two-component system was fully described by Sanchez and de Fontaine,[31] and the extension to multicomponent systems was described in Sanchez *et al.*[32]

The set $\{\xi(r,t)\}$, for the RSM, was approximated numerically by generating a $399 \times 399 \times 399$ site simulation box with ideal NaCl-type ordering of Nb and Mg, randomly changing 1/3 of the Mg ions to Nb, and counting cube-, and cube-subcluster, correlations in the simulation box.

TABLE II. Supercell space group symmetries G, formation energies ΔE (kJ/mol, where mol is the Avogadro's number of a primitive ABO_3 unit cell), and cell parameters.

System	G_{Chem}	ΔE_{Chem}	a	b	c	α	β	γ	G_{SSS}	ΔE_{SSS}	a	b	c	α	β	γ
$[001]_{NNM}$	$P4/mmm$	16.16	3.977	3.977	12.277	90	90	90	Pm	12.27	4.050	3.965	12.250	90	90	89.84
$[110]_{NNM}$	$Amm2$	14.33	5.664	17.087	4.008	90	90	90	Cm	5.50	5.660	16.998	4.092	90	90.68	90
$[111]_{NNM}$	$P\bar{3}m1$	14.11	5.650	5.650	6.941	90	90	120	$P1$	5.33	5.682	5.759	6.964	89.97	90.48	120.43
$[001]_{NCC'}$	$P4/nmm$	11.51	5.646	5.646	12.044	90	90	90	$P1$	2.99	5.645	5.665	12.197	90.15	89.93	89.85
$[111]_{NT}$	$1mmm$	7.66	5.615	17.050	8.022	90	90	90	$P1$	0.00	(5.613	16.995	8.085	89.99	89.85	90.00)[a]

[a]Not the primitive $P1$ cell; 60-atom cell allows comparison with $Immm$ lattice parameters.

TABLE III. Multiplicities and correlation functions for a random distribution; the random-site model (RSM), the five ordered supercells.

Cluster	$M(r,t)$[a]	Random	RSM[b]	[001]	[111]	[110]	$[111]_{NCC'}$	$[111]_{NT}$
0[c]	1	1	1.00000	1	1	1	1	1
i	1	−1/3	−0.33330	−1/3	−1/3	−1/3	−1/3	−1/3
ij	3	1/9	0.10686	5/9	−1/3	1/9	−1/3	−1/9
ik	6	1/9	0.02985	1/9	1/3	−1/9	5/9	0
io	4	1/9	0.06944	−1/3	0	1/3	−1/3	1/3
ijk	12	−1/27	0.03190	−1/3	1/3	−1/9	1/9	2/9
ikn	8	−1/27	0.05100	−1/3	−1/3	1/3	−1/3	0
ijo	24	−1/27	−0.00544	−1/3	0	1/9	1/9	0
ijkl	3	1/81	0.05259	1	−1/3	5/9	1/9	−1/9
ikmo	12	1/81	0.05528	1	1/3	1/9	1/9	−1/9
ijlm	8	1/81	−0.04396	−1/3	−1/3	1/3	−1/3	0
iknp	1	1/81	0.00030	1	−1/3	−1/3	1	1/3
ijlo	24	1/81	−0.03173	5/9	0	−1/3	−1/3	0
ijko	48	1/81	−0.07826	1/9	0	−1/9	1/9	−1/9
ijklm	24	−1/243	−0.02746	−1/3	0	−1/9	1/9	−1/9
ijknp	8	−1/243	−0.00626	−1/3	2/3	1/3	−1/3	−1/3
ijkmo	24	−1/243	0.09270	−1/3	−1/3	1/9	1/9	1/9
ijklmn	12	1/729	0.06074	5/9	1/3	1/9	−1/3	1/9
ijklmo	12	1/729	−0.00138	1/9	−1/3	−1/9	5/9	2/9
jklmnp	8	1/729	−0.28448	−1/3	2/3	1/3	−1/3	−1/3
ijklmno	8	−1/2187	0.01467	−1/3	0	−1/3	−1/3	0
ijklmnop	1	1/6561	−0.04489	1	−1/3	1	1	−1/3
$R_{S\text{-Random}}$[d]		0	0.776	1.165	0.653	0.582	0.690	0.401
$R_{S\text{-RSM}}$		0.776	0	1.297	1.006	1.080	1.201	0.747

[a] $M(r,t)$ is the multiplicity, per site, of the r-body cluster ($r=1,2,\ldots,8$ sites) of type t.
[b] Results from a $399\times399\times399$ site simulation.
[c] The zero- or empty cluster.
[d] $R_{S\text{-Random}}$ is the average (divided by the number of correlation functions, 22) Pythagorean distance between the LASP of structure S, and the LASP for a random alloy; and similarly for $R_{S\text{-RSM}}$.

Because $\overline{\Pi}(r,t)_S$ for any ordered state or random ensemble is a vector, one can unambiguously (except for truncation errors) compare average Pythagorean distances between $\overline{\Pi}(r,t)_S$ for different types of ordering. The last two rows of Table III list average Pythagorean distances relative to the random configuration, $R^{\bullet}_{S\text{-Random}}$, and the RSM, $R_{S\text{-RSM}}$:

$$R_{S\text{-RSM}} = \tfrac{1}{22}\{[M(0)(\xi(0)_S - \xi(0)_{\text{RSM}})]^2 + [M(1)(\xi(1)_S - \xi(1)_{\text{RSM}})]^2 + [M(2,1)(\xi(2,1)_S - \xi(2,1)_{\text{RSM}})]^2 + [M(2,2)(\xi(2,2)_S - \xi(2,2)_{\text{RSM}})]^2 + [M(3,1) \times (\xi(3,1)_S - \xi(3,1)_{\text{RSM}})]^2 + \cdots + [M(8)(\xi(8)_S - \xi(8)_{\text{RSM}})]^2\}^{1/2}. \quad (5)$$

A smaller value of $R_{S\text{-RSM}}$ implies a structure, S, that is more similar to the RSM, so clearly the $[111]_{NT}$ is a better approximate of the RSM than any of the other supercells listed in Fig. 2.

V. STRUCTURALLY STABLE STATES AND LATTICE DYNAMICS

Lattice dynamical force constants were calculated by the frozen phonon method; i.e., in turn, displacing each ion by 0.01 Å in each of the three orthogonal (Cartesian) directions; the force matrix is $R_{i\alpha,j\beta}$; where i and j index ionic positions,

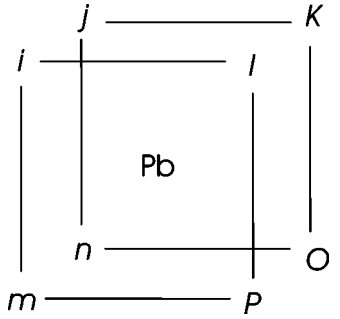

FIG. 4. 8-site configuration.

TABLE IV. The ionic coordinates (in units of a, b, and c, respectively) for the $[111]_{NT}$ supercell [(30 -ion primitive cell, space group $P1$; $a=9.817$, $b=9.816$, $c=5.613$, $\alpha=73.45$, $\beta=73.45$, $\gamma=111.91$].

Type	x	y	z	Type	x	y	z
Mg	0.1700	0.8370	0.4896	Mg	0.8385	0.1711	0.4884
Nb	0.4959	0.4962	0.5017	Nb	0.9937	0.9935	0.0065
Nb	0.6740	0.3384	0.9870	Nb	0.3371	0.6747	0.9865
O	0.9323	0.5741	0.7733	O	0.7420	0.7693	0.2492
O	0.4212	0.1121	0.2513	O	06054	0.9012	0.7715
O	0.0864	0.4443	0.2460	O	0.2739	0.2475	0.7461
O	0.2913	0.7794	0.7056	O	0.6238	0.4465	0.6974
O	0.7316	0.2611	0.2892	O	0.0918	0.9137	0.7774
O	0.4275	0.5719	0.7837	O	0.6086	0.4615	0.2011
O	0.4011	0.5826	0.2947	O	0.2905	0.7932	0.1934
O	0.9600	0.1112	0.7030	O	0.0697	0.9286	0.2809
O	0.7551	0.2377	0.7893	O	0.9528	0.1276	0.1877
Pb	0.9208	0.5699	0.2145	Pb	0.5714	0.9220	0.2120
Pb	0.2194	0.2166	0.2698	Pb	0.7528	0.7623	0.7318
Pb	0.4062	0.0663	0.7244	Pb	0.0590	0.3966	0.7460

α and β are the Cartesian directions. The dynamical matrix DM is $D_{i\alpha,j\beta}=R_{i\alpha,j\beta}/(M_iM_j)^{1/2}$, where M_i is the ith ionic mass. Vibrational mode frequencies were found by diagonalizing the DM, and used to compute IR reflectivity spectra (2):

$$\varepsilon_{\alpha\beta}(\nu)=\varepsilon_{\infty\alpha\beta}+\sum_{\mu}\frac{\varepsilon_{\mu\alpha\beta}\nu_{\mu}^2}{\nu_{\mu}^2-\nu^2+i\gamma_{\mu}\nu}, \tag{6}$$

$$\varepsilon_{\mu\alpha\beta}=\frac{Z_{i\alpha}^{*}Z_{\mu\beta}^{*}}{4\pi^2V\varepsilon_0m_0\nu_{\mu}^2}, \tag{7}$$

$$Z_{\mu\alpha}^{*}=\sum_{i\gamma}Z_{i\alpha\gamma}^{*}(m_0/M_i)^{1/2}a_{\mu i\gamma}. \tag{8}$$

Here V is unit cell volume, M_i atomic mass, $Z_{i\alpha}^{*}$ the Born effective charge, $m_0=1$ atomic mass unit, $\varepsilon_{\infty}=5.83$, the experimental electronic dielectric permittivity, ν is the frequency of the incident radiation, ν_{μ} is the frequency of mode μ, and $a_{\mu i\gamma}$ the component of the DM eigenvector for the μth mode, ith ion, and γ direction. All damping constants were set to 60 cm^{-1}, the approximate average of damping constants that were fit to experimental results (Table I).

A. Ionic relaxation

We first consider the relaxation of ions with respect to ideal perovskite positions in the G_{Chem} structures. In every structure except $[111]_{NNM}$, the largest displacements involve Pb. In $[001]_{NNM}$, the Pb ions with 4 Mg neighbors displace by 0.47 Å toward the $(001)_{\mathrm{Mg}}$ layers in which the O-ions are underbonded (coordinated by two Mg^{2+} ions[33,34]). In $[110]_{NNM}$, the Pb ions with 2 Mg^{2+} neighbors displace by 0.47 Å toward the underbonded O-ion between the 2 Mg^{2+}. The other structures do not contain nearest neighbor Mg-Mg pairs; nonetheless, each Pb ion in an asymmetric environment of Mg and Nb is displaced off-center by a nonzero "local field".[35] The magnitude of these displacements ranges from 0.25 Å to 0.27 Å for the $[001]_{NCC'}$ and $[111]_{NT}$ structures, but is only 0.04 Å for the $[111]_{NNM}$ structure. The small Pb displacements in the $[111]_{NNM}$ structure result because of a special local environment of Pb in this structure. The largest ionic motion is by the Nb-ions, which shift 0.09 Å towards nearest neighbor $(111)_{\mathrm{Mg}}$ planes. In the $[111]_{NT}$ structure, Pb deviates from the [111] axis; a net displacement of $(0.17, 0.17, 0.08)$ Å occurs. Table IV presents the coordinates of the atoms in the relaxed $[111]_{NT}$ structure.

Next, we consider the nature and result of symmetry-breaking relaxations leading to the G_{SSS} structures. All the 15-ion supercells have multiple instabilities. While the dif-

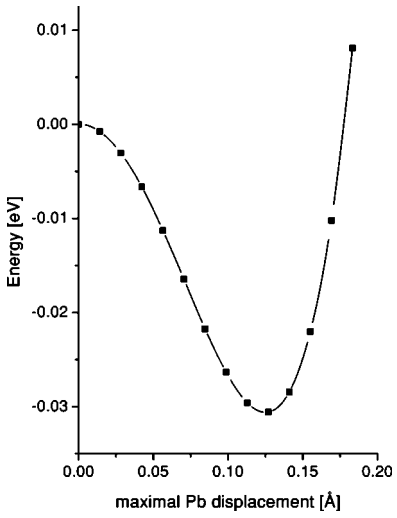

FIG. 5. Computed potential relief for the Last-type soft mode in the $[001]_{NCC'}$ structure.

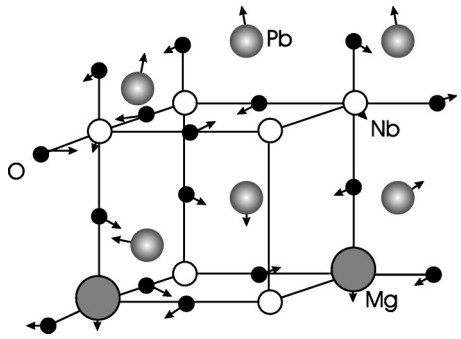

FIG. 6. Atomic shifts in the equilibrium structure of $[111]_{NT}$. The average shift of the Pb ions is approximately along a $[\bar{b}bc]$ direction.

ferent shapes of the supercells studied prevents direct comparison of the modes between the different cells, there are both ferroelectric instabilities of the Last type (Pb motion against the other ions), and antiferrodistortive (tilting) instabilities dominated by O motion. Figure 5 shows the potential barrier for the Last mode in the $[001]_{NCC'}$ structure. With respect to the primitive perovskite cell, every supercell shows wide dispersion of Pb- and O-dominated instabilities across the Brillouin zone. Nb motion opposite O in Nb-O-Nb… chains and planes also plays a role in the FE instabilities. We note, however, that long Nb-O-Nb… chains and planes are unlikely to form experimentally. In the 15-atoms cells, all of the oxygen octahderal tilting angles are between 0° and 4°. In the $[001]_{NCC'}$ structure, one of the checkerboard planes has tilting angles of 10°. In the $[111]_{NT}$ structure, the tilting angles are between 8° and 9° for all octahedra.

Given the existence of multiple instabilities in PMN supercells, it is not surprising that the G_{SSS} states involve the freezing of multiple modes. Figure 6 shows the complexity of the local structure in fully relaxed $[111]_{NT}$. Pair distribution functions (PDF) for the $[001]_{NCC'}$ in $P4/nmm$ (dotted) and $P1$ (solid) structures are shown in Fig. 7. The peak at 2.8 Å is already split by the different Pb displacements in the G_{Chem} structures, and the splitting is significantly enhanced in the G_{SSS} structures. The agreement between the predicted and experimental PDF is quite good.

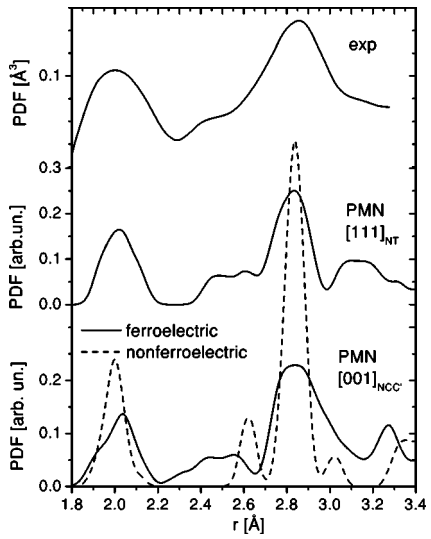

FIG. 7. Computed pair distribution function (PDF) in the $[001]_{NCC'}$ and $[111]_{NT}$ structures of PMN. PDF's are compared with experimental results of Egami *et al.* (Ref. 36).

TABLE V. Estimated polarization (in C/m^2) of structurally stable states of PMN supercells.

Structure	P_x	P_y	P_z	$\lvert P\rvert$
$[001]_{NNM}$	0.525	0.191	0.000	0.558
$[110]_{NNM}$	−0.158	−0.158	−0.547	0.591
$[111]_{NNM}$	0.474	0.476	0.016	0.672
$[001]_{NCC'}$	−0.228	−0.243	0.385	0.509
$[111]_{NT}$	−0.238	−0.221	0.346	0.474
$[111]_{NT}$[a]	−0.212	−0.185	0.288	0.403

[a]Whole matrix of dynamical charges was computed.

We obtained a wide distribution of Pb-O distances in each of the supercells. For instance, in the $[111]_{NT}$ structure, Pb-O distances range between 2.4 Å and 3.3 Å, the shorter Pb-O distances giving rise to the shoulder seen in Fig. 7. Egami *et al.*[36] deduced from their experimental PDF that the Pb ions in PMN are displaced about 0.4 Å from their nominal perovskite positions (assuming that the oxygen ions are fixed). We find, in contrast, that the rms displacement of Pb ions in the fully relaxed structures are only about 0.2 Å. Our results are consistent with the PDF measured by Egami *et al.*, however, because coordinated relaxation of the O ions occurs in a manner which enhances the splitting in the Pb-O distances. The rms displacement of the B cations (Mg;Nb) from nominal perovskite positions is of order 0.1 Å, independent of the Mg-Nb ordering.

We estimate the polarizations of our stable structures by using the displacements of each ion from its position in G_{Chem}, and estimated Born effective charges determined from averaging the calculated Born effective charges for the $[001]_{NCC'}$ structure[37,38]: $Z^*_{\mathrm{Pb}} \approx 4.0$; $Z^*_{\mathrm{Mg}} \approx 2.6$; $Z^*_{\mathrm{Nb}} \approx 7.4$; $Z^*_{\mathrm{O}_\parallel} \approx -4.8$; $Z^*_{\mathrm{O}_\perp} \approx -2.5$. Here the subscripts $\perp$ and $\parallel$ denote the directions of the oxygen displacements perpendicular and parallel to the B-O bond, respectively. The results are shown in Table V. The estimated polarization magnitudes are similar, though about 10% smaller than the zero-temperature polarizations estimated from first principles for $PbTiO_3$ (Ref. 39) and $PbSc_{1/2}Nb_{1/2}O_3$.[40] Remarkably, three of the five structures have SSS polarizations that are pseudomonoclinic (close to an [aab]-type direction).

B. IR Spectra and lattice dynamics of relaxed structures

The IR reflectivity spectra are shown in Fig. 8, and compared with our experiment. We shifted the curves in the figure vertically so to have them all in a compact form. The scale was maintained. The position of the origin can be inferred from the high-frequency minimum position. It is seen that the best agreement between the theory and experiment is for the $[111]_{NT}$ structure. The complex dielectric spectra in

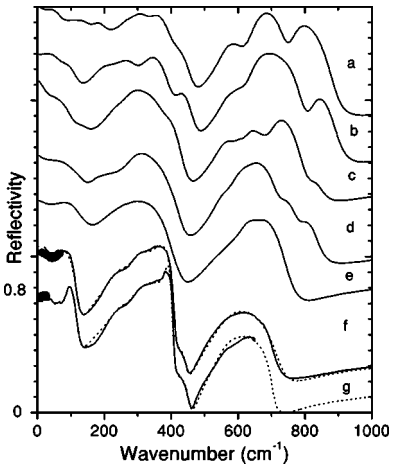

FIG. 8. Computed (a–e) and experimental (f–g) IR reflectivity of PMN: (a) $[001]_{NNM}$; (b) $[011]_{NNM}$; (c) $[111]_{NNM}$; (d) $[001]_{NNC'}$; (e) $[111]_{NT}$; (f) 20 K; (g) 300 K. Dotted lines are damped oscillator model fits (see Table I) to the experimental IR reflectivity spectra (solid lines) and THz spectra (solid points).

the phonon frequency range are plotted in Fig. 9 together with experimental data obtained. We have qualitative agreement for high frequencies. At low frequencies, experiment shows very high values of permittivity connected with relaxations of PNC. These frequencies are below the phonon frequencies. Relaxation contributions to dielectric permittivity were not included in our theoretical consideration (we discussed these problems in a previous publication[41,42]). Notice different scales in the experimental and theoretical plots. The total zone-center phonon density of states of the $[111]_{NCC'}$ and $[111]_{NT}$ structures are shown in Fig. 10. It is seen from this plot that the high energy phonon band is not very dispersive compared to the low frequency bands and compared to the bands known for ABO_3 perovskites. This can be explained by the band folding due to ordering of Mg and Nb.

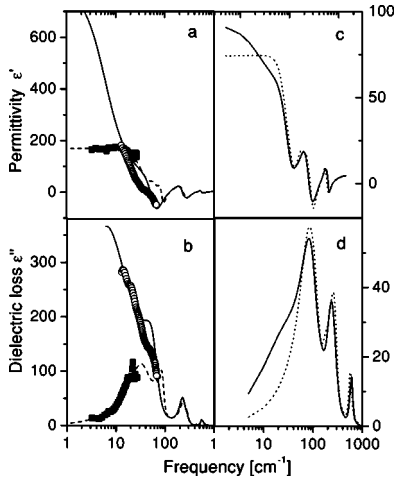

FIG. 9. Experimental (a–b) and computed (c–d) dielectric permittivity and losses: (a–b) circles and squares denote experimental THz data at 300 and 20 K, respectively, the solid and dashed lines are the results of the fits to IR reflectivity at 300 and 20 K, respectively.

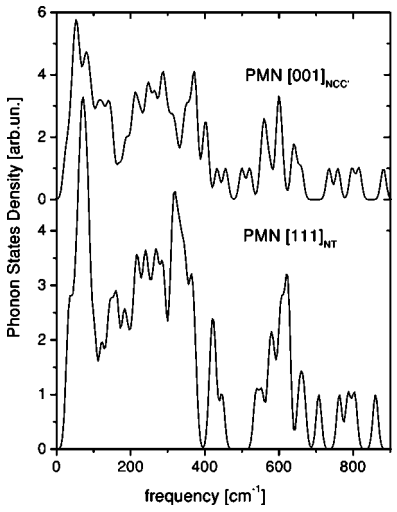

FIG. 10. Computed zone-center phonon density of states in structurally stable states. Three acoustic modes having zero frequency were not included.

Mode assignments were then made at several levels of approximation by averaging the $[111]_{NT}$ DM.[43] The lowest-frequency modes of the supercell are related to the folded acoustic modes of the parent 5-atom cell: excluding zero frequency zone center acoustic modes, eigenvectors of the low-frequency modes in the frequency interval 19–100 cm^{-1} are significant only on Pb. This corresponds to extremely low-frequency acoustic antiphase Pb displacements, which arise due to a very small diagonal element of DM for Pb.

Next, to understand how local 1:1 order may affect the phonon properties, the $[111]_{NT}$ dynamical matrix was averaged with respect to a 1:1 ordered structure. The $[111]_{NT}$ structure is the only one studied which is commensurate with such averaging. Effectively, the $[111]_{Mg_{2/3}Nb_{1/3}}$ layers were treated as though they contained only one average *T*-cation, $T=(Mg_{2/3}Nb_{1/3})$. Symmetry analysis of $[111]_{NT}$ in $Fm\bar{3}m$, yields the following modes: $A_{1g}(R)+E_g(R)+F_{1g}(s)+2F_{2g}(R)+4F_{1u}(IR)+F_{2u}(s)$. Here, IR and *R* indicate IR- and Raman-active modes respectively, and *s* indicates silent. Computed eigenvectors of the $[111]_{NT}$ $P1$ structure were projected onto vectors of the averaged computation to obtain the modes expected to have the highest infrared and Raman activity. The results are shown in Fig. 11, and compared with experimental data from inelastic neutron scattering,[44] Raman scattering and FIR reflectivity measurements (this study).

Polar TO modes $[F_{1u}(\mathrm{IR})]$ are labeled TO1, TO2, TO3, TO4, and TO5. The relative contributions from Pb, T, Nb, $O_{\parallel}$, and $O_{\perp}$ in the TO1 mode (100 cm^{-1}) are: −0.16, 0.21, 0.27, 0.32, and 0.41 Å; where: $O_{\parallel}$ is displaced along B-O bonds; $O_{\perp}$ is displaced perpendicular to B-O bonds.

The TO2 mode at 270 cm^{-1}, is predominately of the Slater-type. Neutron[44] and our IR measurements (Table I) exhibit bands near this frequency. The TO3 and TO4 modes near 340 cm^{-1} are from Nb moving opposite to *T*. Experimental evidence for this band is not definitive, although a mode is found near this frequency in the fit to room-temperature IR data. The TO5 mode near 580 cm^{-1} originates from $O_{\parallel}$-(T, Nb) stretching, and it is clearly observed in the IR and neutron data.

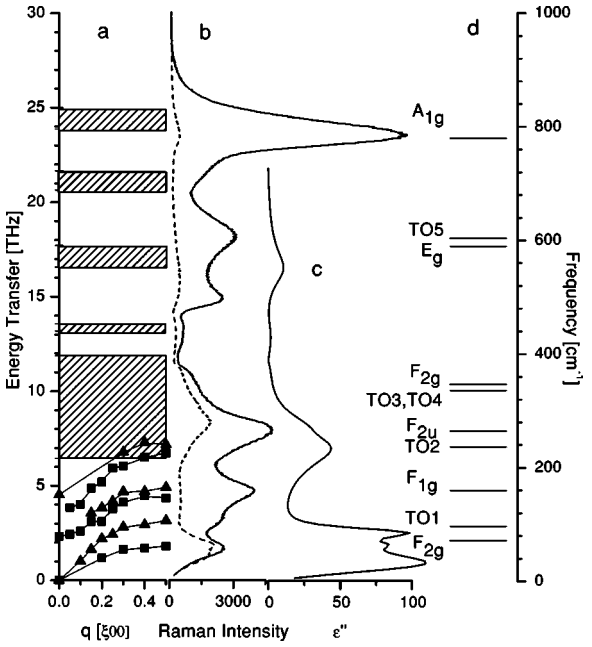

FIG. 11. Comparison of low-temperature experimental data and computational results: (a) 12 K neutron scattering data (Ref. 44) (full triangles and squares correspond to the longitudinal and transverse phonon dispersion branches; the bands show the frequencies of continual neutron scattering); (b) Raman scattering data in two geometries (VV, solid line, and VH, dotted line) recorded at 77 K; (c) dielectric loss $\varepsilon''(\nu)$ obtained from the fit of IR and THz spectra at 20 K; (d) Results of first principles computations in $Fm\bar{3}m$ symmetry.

In first-order Raman scattering from $Fm\bar{3}m$ crystals, A_{1g} and E_g modes should be visible in VV geometry, while F_{2g} modes should be visible in VH geometry. The calculated A_{1g} Raman active mode at 810 cm^{-1} matches quite well the intense peak that is observed experimentally at 780 cm^{-1} in VV spectra. In $[111]_{NT}$ $Fm\bar{3}m$, this mode corresponds to a fully symmetrical, IR inactive, O-breathing mode. The calculated Raman active E_g asymmetrical breathing mode near 590 cm^{-1} is broadened due to local symmetry breaking, and corresponds with experimentally observed bands at 500 and 600 cm^{-1}. In all cases, we had some frequency overlap intervals (and even a multipeak structure) when projecting the modes obtained for GSS onto the modes derived from symmetrized DM.

The calculated Raman active $F_{2g}(2)$ mode near 360 cm^{-1} involves mostly symmetrical $O_\perp$ displacements. A wide envelope of the bands is seen in our Raman experiment at this frequency. The calculated low-frequency F_{2g} Raman mode near 80 cm^{-1} is mostly from Pb displacements. In the VH spectrum, the low-frequency band is a doublet (45 and 62 cm^{-1}). Both components are close to the zone-boundary frequency of the TA branch (50 cm^{-1}) according to neutron scattering data[44] (Fig. 11).

Experimentally, there are strong Raman peaks near 150 cm^{-1} and 250 cm^{-1}. These peaks probably arise from local symmetry breaking (octahedral tilting and/or polar distortions), and not from Nb-T ordering.

VI. DISCUSSION

All the PMN supercells studied here (Fig. 2) are unstable with respect to lower energy structurally stable states, i.e., $\Delta E_{\mathrm{Chem}} > \Delta E_{\mathrm{SSS}}$. Relaxation energies, $\Delta E_{\mathrm{SSS}} - \Delta E_{\mathrm{Chem}}$, are large relative to the thermal vibrational energy, which suggests that local *displacive* symmetry breaking should persist to high temperatures, generating local strain fields. Some instabilities, however, have barriers of the order of thermal energy, especially Last-type modes corresponding to Pb-BO_6 stretching vibrations in finite-size chemically ordered regions. The softest vibrations are exhibited by Pb ions that are coordinated by a highly symmetric array of Mg- and Nb-ions, or Pb ions surrounded by Nb-ions only. Such Pb ions have diagonal Pb-frequencies (the square root of the ratio of the spring constant and mass) of only $\sim$80 cm^{-1}.

Of the supercells studied here, $[111]_{NT}$, in $G_{\mathrm{SSS}} = P1$, has the lowest energy, and with respect to chemical SRO, it is the best approximate of the RSM. This suggests that it is also a good approximate for chemically ordered domains in a PMN crystal with $Pm\bar{3}m$ global symmetry. Egami[45] and Naberezhnov *et al.*[46] reported that the local ferroelectric instability in PMN below the Burns temperature is associated with Pb displacements in opposition to the other ions and this is essentially what occurs in the $[111]_{NT}$ Last-mode dominated FE instability, $Immm \rightarrow P1$. Note, however, that Last-mode-dominated instabilities occur in all five supercells. Computed distributions of the interatomic distances in the 30-ion supercells show that Pb-O distances split into two main groups at 2.5 Å and 3.2 Å, in agreement with experiment.[36]

Computed dynamical charges in PMN are not as large as is typical for simple ABO_3 perovskites:[38] the Nb charge varies from 6.0 to 9.1. An FE-active ion that is surrounded by less FE-active ions, e.g., Nb surrounded by Mg, typically has a reduced dynamical charge, e.g., relative to Nb surrounded by Nb; and the dynamical charge of the less FE-active ion increases (cf. Ref. 37). This happens because charge transfer is reduced when an ion of relatively low electronegativity is surrounded by ions with higher electronegativities.[47]

Computed phonons for all the structures shown in Fig. 8 exhibit three similar features: (1) B-O-B stretching modes at 500–900 cm^{-1}; (2) mixed B-O-B bending and O-B-O stretching modes at 150–500 cm^{-1}; (3) Pb-BO_6 stretching modes at $\nu < 150$ cm^{-1}. Differences between the computed IR spectra for different supercells (Fig. 8) are purely quantitative, not qualitative. The $[111]_{NT}$ spectrum is most similar to the experimental one: the 500–900 cm^{-1} band is relatively narrow, as in the experiment (Fig. 8); but the other computed bands are less intense than their experimental counterparts. This is an artifact of using the same damping constant for all computed modes (60 cm^{-1} is an average of the experimental values). The 60 cm^{-1} damping constant, which we used in our computation, is significantly larger than the usual value for pure perovskites, $\sim$20 cm^{-1}. A large value for disordered PMN is expected because the random fields caused by chemical disorder broaden the phonon density of states. Experimentally, however (cf. Sec. II), some modes exhibited extremely small damping constants, which implies sharper features in the reflectivity spectrum.

Taken together, the first principles results, and experimental data from neutron scattering,[44] Raman, and IR reflectivity enable assignments of specific vibrational modes to experimental phonon peaks. Following Akbas and Davies[8] PMN is approximated as the RSM. Positions of IR-active, Raman-active and silent modes, were calculated, and distribution functions for all these modes have finite width, and some are split.

There are a few low frequency modes in the range $25-95\ \mathrm{cm}^{-1}$ (below the frequency of the soft mode) which are both Raman and IR active. They reflect antiphase Pb displacements[48] that are allowed by the low supercell symmetry, and are all in the acoustic-mode range for the reduced (5-ion) unit cell.

VII. CONCLUSIONS

We studied five ordered supercells of PMN. Instabilities involving Pb off-centering are observed in all supercells and instabilities involving the tilting of O octahedra centered on Mg ions are observed in most. When fully relaxed, the $[111]_{NT}$ structure described here has the lowest known first-principles energy for an ordered PMN structure. It is commensurate with the random site model (RSM) of PMN,[8] and has short-range Mg-Nb correlations that are most comparable to the RSM. Its Raman and IR spectra and pair distribution functions are in qualitative agreement with experiment, allowing mode assignment of the dominant features of the spectra. In its lowest-energy state, it is polarized approximately along a [*bbc*] type direction, yielding pseudomonoclinic symmetry. Unphysical aspects of this perfectly ordered $[111]_{NT}$ supercell as an approximant for the 1:1 ordered regions in experimental PMN, include the lack of a disordered matrix, the fact that there is no experimental evidence for ordering on the $Mg_{2/3}Nb_{1/3}$ sublattice, and the presence of infinite Nb-O-Nb… chains (which influence the lattice dynamics).

ACKNOWLEDGMENTS

Y. Y. and R. S. K. appreciate support by Grant Nos. NSF-DMR-0305588 and NSF-FY2004, S. K. and J. P. support by the Grant Avency of Academy of Sciences (Project Nos. A1010203 and AVOZ1-010-914), Grant Agency of Czech Republic (Project No. 202/04/0993) and ministry of Education of the Czech Republic (Project No. COST OC525.20/00) S.S.P. grants r.u.01.01.037 ("Russian Universities") and 04-02-16103 (RFBR). S.B.V. acknowledges RFBR 02-02-16695 and CRDF RP1-2361-ST-02.

*Also at Physics Department, Rostov State University, 5 Zorge Street, 344090 Rostov on Don, Russia.

[1] G. A. Smolenskii, V. A. Bokov, V. A. Isupov, N. N. Krainik, R. E. Pasynkov, and A. I. Sokolov, *Ferroelectrics and Related Materials* (Gordon and Breach, New York, 1984).
[2] L. E. Cross, Ferroelectrics **76**, 241 (1987).
[3] H. B. Krause, J. M. Cowley, and J. Wheatley, Acta Crystallogr., Sect. A: Cryst. Phys., Diffr., Theor. Gen. Crystallogr. **A35**, 1015 (1979).
[4] E. Husson, M. Chubb, and A. Morell, Mater. Res. Bull. **23**, 357 (1988).
[5] E. Husson, L. Abello, and A. Morell, Mater. Res. Bull. **25**, 539 (1990).
[6] F. S. Galasso, *Structure, Properties, and Preparation of Perovskite Compounds* (Pergamon, Oxford, 1969).
[7] H. B. Krause and D. L. Gibbon, Z. Kristallogr. **134**, 44 (1971).
[8] M. A. Akbas and P. K. Davies, J. Am. Ceram. Soc. **80**, 2933 (1997).
[9] P. K. Davies and M. A. Akbas, J. Phys. Chem. Solids **61**, 159 (2000).
[10] P. K. Davies, L. Farber, M. Valant, and M. A. Akbas, in *Fundamental Physics of Ferroelectrics, 2000*, edited by R. E. Cohen (AIP, New York, 2000), Vol. 535, p. 38.
[11] G. Burns and F. H. Dacol, Solid State Commun. **48**, 853 (1983).
[12] H. G. Jin, J. Zhu, S. Miao, X. W. Zhang, and Z. Y. Cheng, J. Appl. Phys. **89**, 5048 (2001).
[13] S. Miao, J. Zhu, X. Zhang, and Z. Y.Cheng, Phys. Rev. B **65**, 052101 (2002).
[14] A. A. Karamyan, Sov. Phys. Solid State **18**, 1861 (1977).
[15] I. M. Reaney, J. Petzelt, V. V. Voitsekhovskii, F. Chu, and N. Setter, J. Appl. Phys. **76**, 2086 (1994).
[16] I. G. Siny, R. S. Katiyar, and A. S. Bhalla, Ferroelectr. Rev. **2**, 51 (2000).
[17] O. Svitelskiy, J. Toulouse, G. Yong, and Z.-G. Ye, Phys. Rev. B **68**, 104107 (2003).
[18] H. Idink and W. White, J. Appl. Phys. **76**, 1789 (1994).
[19] V. Bovtun, S. Kamba, A. Pashkin, M. Savinov, P. Samoukhina, J. Petzelt, I. P. Bykov, and M. D. Glinchuk, Ferroelectrics **298**, 23 (2004).
[20] V. P. Bovtun and M. A. Leshchenko, Ferroelectrics **190**, 185 (1997).
[21] A. Levstik, Z. Kutnjak, C. Filipič, and R. Pirc, Phys. Rev. B **57**, 11 204 (1998).
[22] G. A. Smolensky, I. G. Siny, R. V. Pisarev, and E. G. Kuzminov, Ferroelectrics **12**, 135 (1976).
[23] S. Kamba, E. Buixaderas, J. Petzelt, J. Fousek, J. Nosek, and P. Bridenbaugh, J. Appl. Phys. **93**, 933 (2003).
[24] G. Kresse and J. Hafner, Phys. Rev. B **47**, 558 (1993).
[25] G. Kresse and J. Furthmüller, Phys. Rev. B **54**, 11 169 (1996).
[26] D. Vanderbilt, Phys. Rev. B **41**, 7892 (1990).
[27] B. P. Burton, R. P. McCormack, B. H. Toby, and E. K. Goo, Ferroelectrics **194**, 187 (1997).
[28] S.-H. Wei, L. G. Ferreira, J. E. Bernard, and A. Zunger, Phys. Rev. B **42**, 9622 (1990).
[29] Z. W. Lu, S.-H. Wei, A. Zunger, S. Frota-Pessoa, and L. G. Ferreira, Phys. Rev. B **44**, 512 (1991).
[30] Z. W. Lu, S.-H. Wei, and A. Zunger, Phys. Rev. B **44**, 10 470 (1991).
[31] J. M. Sanchez and D. deFontaine, Phys. Rev. B **21**, 216 (1980).
[32] J. M. Sanchez, F. Ducastelle, and D. Gratias, Physica A **128**, 334

(1984).
[33] B. P. Burton and E. Cockayne, Phys. Rev. B **60**, R12 542 (1999).
[34] B. P. Burton, Modell. Simul. Mater. Sci. Eng. **8**, 211 (2000).
[35] U. V. Waghmare, E. Cockayne, and B. P. Burton, Ferroelectrics **291**, 187 (2003).
[36] T. Egami, E. Mamontov, W. Dmowski, and S. B. Vakhrushev, in *Fundamental Physics of Ferroelectrics 2003*, edited by P. K. Davies and D. J. Singh (AIP, New York, 2003), Vol. 677, p. 48.
[37] S. Prosandeev, E. Cockayne, and B. Burton, in *Fundamental Physics of Ferroelectrics 2002*, edited by R. E. Cohen (AIP, New York, 2002), Vol. 626, p. 64; cond-mat/0208316.
[38] S. Prosandeev, E. Cockayne, and B. Burton, in *Fundamental Physics of Ferroelectrics 2003*, edited by P. K. Davies and D. J. Singh (AIP, New York, 2003), Vol. 677, p. 146; cond-mat/0303015; cond-mat/0404349.
[39] U. V. Waghmare and K. M. Rabe, Phys. Rev. B **55**, 6161 (1997).
[40] E. Cockayne, B. P. Burton, and L. Bellaiche, in *Fundamental Physics of Ferroelectrics 2001*, edited by Henry Krakauer, AIP Conf. Proc. No. 582 (American Institute of Physics, Melville, NY, 2001), p. 191.
[41] S. Prosandeev, E. Cockayne, B. Burton, V. Trepakov, S. Kapphan, M. Savinov, and L. Jastrabik, Jpn. J. Appl. Phys., Part 1 **41**, 7179 (2002).
[42] S. A. Prosandeev, E. Cockayne, and B. P. Burton, Phys. Rev. B **68**, 014120 (2003).
[43] To average the dynamical matrix of a supercell of symmetry G_1 with respect to a structure of symmetry G_2 (G_1 a subgroup of G_2), apply all g_2 rotational and translational symmetry elements of G_2 to the dynamical matrix, take the sum, and divide by the number g_2 of the symmetry elements in G_2.
[44] B. Dorner, A. S. Ivanov, S. Vakhrushev, S. Lushnikov, S. Gvasaliya, D. Strauch, and K. Schmalzl, Ferroelectrics **282**, 9 (2003).
[45] T. Egami, Ferroelectrics **267**, 101 (2002).
[46] A. Naberezhnov, S. Vakhrushev, B. Dorner, D. Strauch, and H. Moudden, Eur. Phys. J. B **11**, 13 (1999).
[47] I. P. Raevskii, S. A. Prosandeev, and I. A. Osipenko, Phys. Status Solidi B **198**, 695 (1996).
[48] A. Tkachuk, in *Fundamental Physics of Ferroelectrics 2003*, edited by P. K. Davies and D. J. Singh (AIP, New York, 2003), Vol. 677, p. 55.